A variable kinematic model for the prediction of capacitance variations in embedded PZT sensors

A VARIABLE KINEMATIC MODEL FOR THE PREDICTION OF CAPACITANCE VARIATIONS IN EMBEDDED PZT SENSORS

Journal of Intelligent Material Systems and Structures
XX(X):1–15

DOI: 10.1177/ToBeAssigned
www.sagepub.com/
SAGE

Jamal Najd[1,2], Enrico Zappino[1,*], Erasmo Carrera[1], Walid Harizi [2] and Zoheir Aboura [2]

Abstract

This paper proposes the use of a two-dimensional refined finite element model, based on the Carrera Unified Formulation (CUF), to predict the variation in capacitance of embedded piezoelectric sensors. The accurate stress field of laminated structures with embedded sensors has been evaluated by exploiting the capabilities of refined layer-wise models. A fully coupled electro-mechanical formulation has been adopted to predict the piezoelectric response of embedded sensors. Different piezoelectric materials have been considered and a parametric analysis has been carried out including geometrical and physical parameters. The results show that the variation in capacitance is highly affected by the through-the-thickness deformations, that is, classical models cannot be used to predict this phenomenon. The variation in the capacitance value has been confirmed by experimental results proposed in the literature and can be used as a parameter for evaluating the internal stress field.

Keywords

Plate model, Layer-Wise model, Carrera Unified Formulation, Embedded piezo-sensor, Capacitance change

Introduction

Composite structures are known to be light materials with a high mechanical strength. This combination allows composites to be widely used in the design of high-performance structures for specific applications such as aeronautical and space applications. Composite materials offer the optimal conditions for embedding as the devices can be positioned between the laminae during manufacturing. This ensures a strong bonding of the sensor with the structure (Shin et al. 2016). However, the manufacturing of smart structures is quite cumbersome, with the temperature limitation during manufacturing as it should be below the Curie temperature of the sensor (N. Ghasemi-Nejhad et al. 2005). Many techniques have been developed for manufacturing smart polymeric composites (Tuloup et al. 2019). On the other side, the uncertainties that lie behind the prediction of composite structural failure lead to an over-sizing in the structures to insure the safe performance. For the sake of structural monitoring, the use of a network of sensors can provide a description of the mechanical stress field in the structure and can be used to predict or to prevent the collapse of the whole structure (Tuloup et al. 2020). Piezoelectric sensors are considered as a primary option for this application. They can be used to help in identifying the structural damage by

[1] Mul2 Group, Department of Mechanical and Aerospace Engineering, Politecnico di Torino, Corso Duca degli Abruzzi 24, 10129 Torino, Italy
[2] Université de technologie de Compiègne, Roberval (Mechanics energy and electricity), Centre de recherche Royallieu - CS 60 319 - 60 203 Compiègne Cedex - France

Corresponding author:
E. Zappino, Department of Mechanical and Aerospace Engineering, Politecnico di Torino, Corso Duca degli Abruzzi 24, 10129 Torino, Italy.
Email: enrico.zappino@polito.it

generating lamb waves (Tang et al. 2011; Su et al. 2006a,b). They can be either surface mounted or embedded (in-situ) in the structure (M. Yaqoob et al. 2010; Reddy 1999) and their capabilities vary between active or passive sensing (Nasrollahi et al. 2018). It has been proven that when embedded, the effectiveness of the piezoelectric device increases, compared to a surface mounted one (Zappino and Carrera 2020) while providing a better protection to the device from external and environmental factors during its operational life cycle. Embedding piezoelectric sensors into composite laminated structures lead to obtaining a smart structure with sensing and actuating abilities, with the same light-density material, high mechanical and thermal properties. This, on the other hand, often comes at the expense of a complex stress concentration around the embedded area at the position of the transducer (Zappino and Carrera 2020) which explains the higher coupling and better sensibility but degrading the strength of the structure at that position. On top of the subjection to a complex stress field, embedding can lead to non-fixed sensor properties, e.g., capacitance. Capacitance variation is of great importance in energy harvesting applications, as the power output is inversely proportional to the capacitance, which in turn depends on the stiffness of the host structure and the properties of the piezoelectric material (Elvin et al. 2018). In health monitoring applications, the prediction of the variation of the sensor properties is of great importance as these changes can give an idea about the current health of the structure. For example, Najd et al. (2022) studied estimating the fatigue limit in polymer-matrix composites through measuring the capacitance variation of embedded piezoelectric transducers (PVDF) under self-heating tests. Elvin et al. (2018) investigated the capacitance variation by using an axisymmetric FEM model and then proposed an equivalent spring model split between a horizontal and a vertical spring model.

In order to accurately estimate the stresses developed in the structure, mainly at the position of the embedded piezo-transducer, it is necessary to use a numerical tool that takes into account the through-the-thickness stresses, even when using a plate model. Unfortunately, commercial numerical tools are unable to fulfil this constraint (Carrera and Zappino 2018) due to two main limitations. First, in order to use a coupled piezoelectric analysis, it is essential to use a 3D finite element model, which leads to a high computational cost. Second, even if a plate model was used in some specific areas where only a mechanical problem is modelled to decrease the computational cost and a 3D model was used at the location of the piezoelectric problem (locally refined model), the limitations of the kinematic model used, such as the Classical Plate Theory (CPT) and the First-order Shear Deformation Theory (FSDT) often lead to inaccurate shear stresses and through-the-thickness displacement variables which is reflected on the stresses distribution through-the-thickness, that in turn lead to inaccurate results in the 3D model. This plate modelling approach is an equivalent single layer approach, where the composite laminate is estimated to be composed of a single layer with the corresponding equivalent stiffness. Though it is less computationally expensive, it neglects the zig-zag effect between each lamina. Different Higher Order Theories (HOT) were suggested in order to improve the accuracy of plate models (Reddy 2004, 1984). Based on that, the Carrera Unified Formulation (Carrera 2003; Carrera et al. 2014) was introduced to obtain refined plate models to treat thin-wall structures problems in a unified manner.

In the first part of this paper, the Carrera Unified Formulation (CUF) is introduced for 2D plate models. In the second part an assessment of the plate Layer-Wise (LW) numerical model was carried out. The third part presents the results of capacitance variation in piezoelectric sensors when embedded. These results were compared to numerical and experimental results from the literature.

Refined two-dimensional electro-mechanical models

In this section the governing equations of higher order two-dimensional models are introduced and extended to the piezo-electric problem.

Preliminaries

Considering the electric potential ϕ as a primary variable in a coupled piezoelectric model, a generalised 4×1 displacement vector $\boldsymbol{q}$ can be adopted:

$$\boldsymbol{q} = \{u_x, u_y, u_z, \phi\}^T \tag{1}$$

where the subscript T denotes the transpose of a matrix.

The 3×1 electric field vector $\boldsymbol{E}$ can be derived as:

$$\boldsymbol{E} = \{E_x, E_y, E_z\}^T = \{\partial_x, \partial_y, \partial_z\}^T \phi \tag{2}$$

The generalized 9×1 strain vector, $\bar{\varepsilon}$, can be written as:

$$\bar{\varepsilon} = \{\varepsilon_{xx}, \varepsilon_{yy}, \varepsilon_{zz}, \varepsilon_{xz}, \varepsilon_{yz}, \varepsilon_{xy}, E_x, E_y, E_z\}^T = \bar{\boldsymbol{D}}\boldsymbol{q} \tag{3}$$

where the general matrix of the differential operator $\bar{\boldsymbol{D}}$ is a 9×4 matrix given by:

$$\bar{\boldsymbol{D}} = \begin{bmatrix} \frac{\partial}{\partial x} & 0 & 0 & 0 \\ 0 & \frac{\partial}{\partial y} & 0 & 0 \\ 0 & 0 & \frac{\partial}{\partial z} & 0 \\ \frac{\partial}{\partial z} & 0 & \frac{\partial}{\partial x} & 0 \\ 0 & \frac{\partial}{\partial z} & \frac{\partial}{\partial y} & 0 \\ \frac{\partial}{\partial y} & \frac{\partial}{\partial x} & 0 & 0 \\ 0 & 0 & 0 & -\frac{\partial}{\partial x} \\ 0 & 0 & 0 & -\frac{\partial}{\partial y} \\ 0 & 0 & 0 & -\frac{\partial}{\partial z} \end{bmatrix} \tag{4}$$

In the case of the principle of virtual displacement (PVD), the electromechanical constitutive equations (stress - charge form or *e-form*) can be expressed by:

$$\begin{aligned} \boldsymbol{\sigma} &= \boldsymbol{C}^E \boldsymbol{\varepsilon} - \boldsymbol{e}^T \boldsymbol{E} \\ \boldsymbol{D}_e &= \boldsymbol{e}\boldsymbol{\varepsilon} + \boldsymbol{\chi}^S \boldsymbol{E} \end{aligned} \tag{5}$$

in which $\boldsymbol{D}_e$ is a 3×1 the electric displacement vector $\{D_x, D_y, D_z\}^T$, $\boldsymbol{\sigma}$ is the 6×1 mechanical stress vector, $\boldsymbol{C}$ is a 6×6 matrix of mechanical material coefficients (Stiffness matrix) and $\boldsymbol{\varepsilon}$ is the 6×1 strain vector. The superscripts E and S denote that the terms are evaluated at a constant electric field and strain respectively. The 3×3 dielectric permittivity matrix evaluated at constant stress $\boldsymbol{\chi}^S$ will appear like:

$$\boldsymbol{\chi}^S = \begin{bmatrix} \chi_{11}^S & \chi_{12}^S & 0 \\ \chi_{21}^S & \chi_{22}^S & 0 \\ 0 & 0 & \chi_{33}^S \end{bmatrix} \tag{6}$$

and the piezoelectric stiffness coefficient matrix $\boldsymbol{e}$ is a 3×6 matrix given by:

$$\boldsymbol{e} = \begin{bmatrix} e_{11} & e_{12} & e_{13} & e_{14} & e_{15} & e_{16} \\ e_{21} & e_{22} & e_{23} & e_{24} & e_{25} & e_{26} \\ e_{31} & e_{32} & e_{33} & e_{34} & e_{35} & e_{36} \end{bmatrix} \tag{7}$$

The generalized 9×1 stress vector $\bar{\boldsymbol{\sigma}}$ can be seen as:

$$\bar{\boldsymbol{\sigma}} = \{\sigma_{xx}, \sigma_{yy}, \sigma_{zz}, \sigma_{xz}, \sigma_{yz}, \sigma_{xy}, D_x, D_y, D_z\}^T \tag{8}$$

The generalized stress vector can be written as in Equation 9, which in a more compact form can be expressed as:

$$\bar{\boldsymbol{\sigma}} = \tilde{\boldsymbol{H}}\bar{\boldsymbol{\varepsilon}} \tag{10}$$

If the piezoelectric components are poled in the third material axis, the dielectric permittivity matrix $\boldsymbol{\chi}^S$ becomes:

$$\boldsymbol{\chi}^S = \begin{bmatrix} \chi_{11}^S & 0 & 0 \\ 0 & \chi_{22}^S & 0 \\ 0 & 0 & \chi_{33}^S \end{bmatrix} \tag{11}$$

and the piezoelectric stiffness coefficient matrix $\boldsymbol{e}$ would be in the following form:

$$\boldsymbol{e} = \begin{bmatrix} 0 & 0 & 0 & e_{15} & 0 & 0 \\ 0 & 0 & 0 & 0 & e_{24} & 0 \\ e_{31} & e_{32} & e_{33} & 0 & 0 & 0 \end{bmatrix} \tag{12}$$

For more details about the rotation of piezoelectric material coefficient matrices the reader is referred to Kpeky et al. (2017); Kapuria and Hagedorn (2007); Benjeddou et al. (1997).

CUF-based plate elements with node-dependent kinematics

In this section, the refined two-dimensional plate models for electromechanical analysis are presented. The reference coordinate system is as shown in Figure 1. First, plate models in the mechanical case can be refined using the CUF by further expanding a generic function $F_\tau(z)$ defined to the thickness of the plate, leading to the following

$$\begin{Bmatrix} \sigma_{xx} \\ \sigma_{yy} \\ \sigma_{zz} \\ \sigma_{xz} \\ \sigma_{yz} \\ \sigma_{xy} \\ D_x \\ D_y \\ D_z \end{Bmatrix} = \begin{bmatrix} C_{11}^E & C_{12}^E & C_{13}^E & 0 & 0 & C_{16}^E & -e_{11} & -e_{21} & -e_{31} \\ C_{21}^E & C_{22}^E & C_{23}^E & 0 & 0 & C_{26}^E & -e_{12} & -e_{22} & -e_{32} \\ C_{31}^E & C_{32}^E & C_{33}^E & 0 & 0 & C_{36}^E & -e_{13} & -e_{23} & -e_{33} \\ 0 & 0 & 0 & C_{44}^E & C_{45}^E & 0 & -e_{14} & -e_{24} & -e_{34} \\ 0 & 0 & 0 & C_{54}^E & C_{55}^E & 0 & -e_{15} & -e_{25} & -e_{35} \\ C_{61}^E & C_{62}^E & C_{63}^E & 0 & 0 & C_{66}^E & -e_{16} & -e_{26} & -e_{36} \\ e_{11} & e_{12} & e_{13} & e_{14} & e_{15} & e_{16} & \chi_{11}^S & \chi_{12}^S & 0 \\ e_{21} & e_{22} & e_{23} & e_{24} & e_{25} & e_{26} & \chi_{21}^S & \chi_{22}^S & 0 \\ e_{31} & e_{32} & e_{33} & e_{34} & e_{35} & e_{36} & 0 & 0 & \chi_{33}^S \end{bmatrix} \begin{Bmatrix} \varepsilon_{xx} \\ \varepsilon_{yy} \\ \varepsilon_{zz} \\ \varepsilon_{xz} \\ \varepsilon_{yz} \\ \varepsilon_{xy} \\ E_x \\ E_y \\ E_z \end{Bmatrix} \tag{9}$$

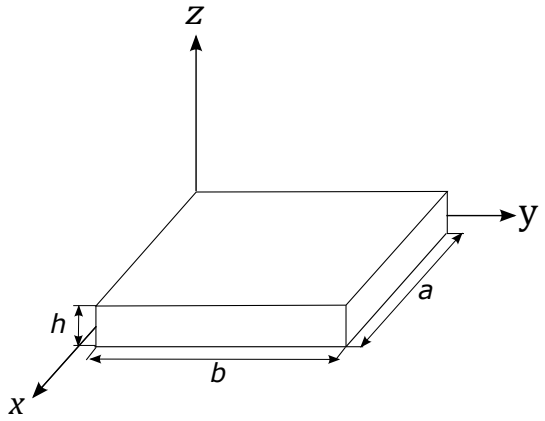

Figure 1. Geometry and reference system of a 2D plate model

expression:

$$\boldsymbol{u} = F_\tau(z)\boldsymbol{u}_\tau(x,y) \qquad \tau = 0, \cdots, N. \tag{13}$$

in which M represents the number of expansion terms. $\boldsymbol{u} = \{u, v, w\}^T$ is the mechanical displacement vector, and $\boldsymbol{u}_\tau(x,y)$ is a vector of unknown displacements defined on the neutral plane of the plate. By extending Equation 13 into the electromechanical case, one can obtain:

$$\boldsymbol{q} = F_\tau(z)\boldsymbol{q}_\tau(x,y) \qquad \tau = 0, \cdots, N. \tag{14}$$

with $\boldsymbol{q} = \{u, v, w, \phi\}^T$ as the generalized electromechanical displacement vector. Various theories can be adopted to define the through-the-thickness functions $F_\tau(z)$. In the analysis of multi-layered structures, Taylor-like expansions apply to Equivalent Single Layer (ESL) approaches, while Lagrange-type expansions suit the Layer-Wise (LW) models. When CUF-based functions are applied to the thickness to formulate the plate elements, the planar unknown vector $\boldsymbol{q}_\tau(x,y)$ can be approximated by the Lagrangian shape functions $N_i(x,y)$ as follows:

$$\begin{aligned} \boldsymbol{q} &= N_i(x,y)F_\tau(z)\boldsymbol{q}_{i\tau}(x,y) \\ \tau &= 0, \cdots, N; i = 1, \cdots, M. \end{aligned} \tag{15}$$

where F_τ represent the node kinematics of a plate element. All the numerical plate models presented in this work are built up using the conventional 9 node plate elements with their corresponding traditional Lagrangian shape function. As the models presented only use a Layer-wise modelling approach, the formulation of Lagrange Expansions was exclusively presented.

Nodal kinematics with Lagrange Expansions (LE)

The through-the-thickness functions can be constructed using Lagrange interpolation polynomials, which leads to LE-type kinematics. Taking the Lagrange interpolation polynomials on the top and bottom points of a linear element (B2) as an example, the expansion can be expressed as:

$$\begin{cases} u = F_1 u_1 + F_2 u_2 \\ v = F_1 v_1 + F_2 v_2 \\ w = F_1 w_1 + F_2 w_2 \\ \phi = F_1 \phi_1 + F_2 \phi_2 \end{cases} \tag{16}$$

where (u_1, v_1, w_1, ϕ_1) and (u_2, v_2, w_2, ϕ_2) are the electromechanical displacement components at the top and the bottom of the plate, and F_1, F_2 are linear Lagrange functions expressed as:

$$F_1 = \frac{1+\zeta}{2}$$
$$F_2 = \frac{1-\zeta}{2} \tag{17}$$

where $-1 < \zeta < 1$, and where the functions F are used in the natural thickness coordinate of the plate. Note that the Lagrange functions have the following unique properties:

$$F_1 = 1, \quad F_2 = 0 \quad for \quad \zeta = 1$$
$$F_1 = 0, \quad F_2 = 1 \quad for \quad \zeta = -1 \tag{18}$$

Unlike Taylor Expansion (TE) were ESL approaches are used, when using displacement-based LE models, the degrees of freedom of the FEM models are the actual physical translational displacements of the through-the-thickness nodes. Using LE expansions allow the continuity of transverse shear stresses at the interfaces and permit the approximation of zig-zag distribution of shear deformation. It can be referred to Carrera et al. (2011b) and Carrera et al. (2014) for more details. In the work of this paper, the mentioned through-the-thickness expansion B2, B3 and B4 elements represent respectively the linear, quadratic and cubic expansion elements.

Electro-mechanical governing equation of node-dependent kinematic plate elements

By applying the principle of virtual displacement (PVD) it is possible to derive the stiffness of the plate elements, as well as the external load vector. Substituting the constitutive equations, the following expression can be obtained:

$$\delta L_{int} = \int_V \delta \bar{\boldsymbol{\varepsilon}}^T \bar{\boldsymbol{\sigma}} dV = \delta L_{ext} \tag{19}$$

If the geometrical relations and shape functions derived earlier are substituted into the above expression, one can obtain:

$$\delta L_{int} = \delta \boldsymbol{q}_{sj} \int_V N_j F_s^j \bar{\boldsymbol{D}}^T \tilde{\boldsymbol{H}} \bar{\boldsymbol{D}} F_\tau^i N_i dV \boldsymbol{q}_{i\tau} \tag{20}$$

In a more compact form, the above expression can be written as:

$$\delta L_{int} = \delta \boldsymbol{q}_{sj}^T \boldsymbol{K}_{ij\tau s} \boldsymbol{q}_{\tau i} \tag{21}$$

in which $\boldsymbol{K}_{ij\tau s}$ is a 4×4 stiffness matrix, containing the *fundamental nuclei* (FNs), and it can be expressed as:

$$\boldsymbol{K}_{ij\tau s} = \int_V N_j F_s^j \bar{\boldsymbol{D}}^T \tilde{\boldsymbol{H}} \bar{\boldsymbol{D}} F_\tau^i N_i dV \tag{22}$$

The virtual work due to the external load $\boldsymbol{P} = \{P_x, P_y, P_z, P_\phi\}$ is expressed by:

$$\delta L_{ext} = \int_V \delta \boldsymbol{q}^T \boldsymbol{P} dV \tag{23}$$

Considering the displacement function Equation 15, the external work can be written as:

$$\delta L_{ext} = \delta \boldsymbol{q}_{sj}^T \int_V F_s^j N_j \boldsymbol{P} dV = \delta \boldsymbol{q}_{sj}^T \cdot \boldsymbol{p}_{sj} \tag{24}$$

where $\boldsymbol{p}_{sj}$ is the expression of the load vector for FEM. Then the governing equation for a static problem can be expressed as:

$$\delta \boldsymbol{q}_{sj} : \quad \boldsymbol{K}_{ij\tau s} \cdot \boldsymbol{q}_{\tau i} = \boldsymbol{p}_{sj} \tag{25}$$

For additional information regarding the components of the individual terms in the fundamental nucleus of the stiffness matrix, it can be referred to Carrera et al. (2011a)

Capacitance Variation: Governing Equations

Reinstating the electromechanical constitutive equations (*e-form*) given by (5)

$$\boldsymbol{\sigma} = \boldsymbol{C}^E \boldsymbol{\varepsilon} - \boldsymbol{e}^T \boldsymbol{E}$$
$$\boldsymbol{D}_e = \boldsymbol{e}\boldsymbol{\varepsilon} + \boldsymbol{\chi}^S \boldsymbol{E} \tag{26}$$

After manipulating the first term, one can get:

$$\left[\boldsymbol{C}^E\right]^{-1} \boldsymbol{\sigma} = \boldsymbol{\varepsilon} - \left[\boldsymbol{C}^E\right]^{-1} \boldsymbol{e}^T \boldsymbol{E} \tag{27}$$

which gives

$$\boldsymbol{\varepsilon} = \left[\boldsymbol{C}^E\right]^{-1} \boldsymbol{\sigma} + \left[\boldsymbol{C}^E\right]^{-1} \boldsymbol{e}^T \boldsymbol{E} \tag{28}$$

substituting (28) into the second term of (26) and rearranging, one can obtain:

$$\boldsymbol{D}_e = \boldsymbol{e}\left[\boldsymbol{C}^E\right]^{-1}\boldsymbol{\sigma} + (\boldsymbol{e}\left[\boldsymbol{C}^E\right]^{-1}\boldsymbol{e}^T + \boldsymbol{\chi}^S)\boldsymbol{E} \tag{29}$$

Assembling (28) and (29), the general constitutive equations of a piezoelectric problem (*d-form*) in matrix notation can be obtained in (30) :

$$\begin{aligned} \boldsymbol{\varepsilon} &= \boldsymbol{s}^E\boldsymbol{\sigma} + [\boldsymbol{d}]^T\boldsymbol{E} \\ \boldsymbol{D}_e &= [\boldsymbol{d}]\boldsymbol{\sigma} + [\boldsymbol{\chi}]^t\boldsymbol{E} \end{aligned} \tag{30}$$

where $\boldsymbol{\sigma}$ and $\boldsymbol{\varepsilon}$ are 6×1 stress and strain component vectors respectively, $\boldsymbol{s}$ is the 6×6 compliance matrix of transversely orthotropic materials of the transducer, $\boldsymbol{d}$ is the 3×6 electromechanical coupling matrix, $\boldsymbol{E}$ is a 3×1 electric field vector, D is a 3×1 electric displacement vector, $\boldsymbol{\chi}$ is a 3×3 permittivity matrix, the subscript T denotes the transpose of a matrix and the superscripts E and t denote that the corresponding terms are evaluated at a constant electric field and stress respectively. For a simplified case where d_{15} = d_{24} = 0, and where the piezoelectric is poled in the 3-direction and having its 1-2 plane parallel faces coated with electrodes, with the 3-axis as an axis of symmetry and the electric field is only to the thickness direction, the expanded form of the equation becomes (31):

$$\begin{Bmatrix} \varepsilon_1 \\ \varepsilon_2 \\ \varepsilon_3 \\ \varepsilon_4 \\ \varepsilon_5 \\ \varepsilon_6 \\ D_3 \end{Bmatrix} = \begin{bmatrix} s_{11}^E & s_{12}^E & s_{13}^E & 0 & 0 & 0 & d_{31} \\ s_{12}^E & s_{11}^E & s_{13}^E & 0 & 0 & 0 & d_{31} \\ s_{13}^E & s_{13}^E & s_{33}^E & 0 & 0 & 0 & d_{33} \\ 0 & 0 & 0 & s_{44}^E & 0 & 0 & 0 \\ 0 & 0 & 0 & 0 & s_{55}^E & 0 & 0 \\ 0 & 0 & 0 & 0 & 0 & s_{66}^E & 0 \\ d_{31} & d_{31} & d_{33} & 0 & 0 & 0 & \chi_{33}^t \end{bmatrix} \begin{Bmatrix} \sigma_1 \\ \sigma_2 \\ \sigma_3 \\ \sigma_4 \\ \sigma_5 \\ \sigma_6 \\ E_3 \end{Bmatrix} \tag{31}$$

where s_{ij} are the elements of the compliance matrix, d_{ij} are the electromechanical coupling terms, D_3 and E_3 are the 3-direction electrical displacement and electric fields respectively. The capacitance of an embedded piezoelectric with surface parallel electrodes was given in Elvin et al. (2018) in a cylindrical coordinate system. Transforming the equations to the Cartesian coordinate system, the embedded/ blocked capacitance becomes (32):

$$C = \frac{Q}{V} = \frac{\oint_A D_z dx dy}{V} \tag{32}$$

where Q is the free charge.

substituting the value of the electrical displacement from (31) in (32), we get:

$$C = \frac{\iint_A (d_{31}\sigma_1 + d_{31}\sigma_2 + d_{33}\sigma_3) \; + (\chi_{33}^t \cdot V/t)\, dx\, dy}{V} \tag{33}$$

where V is the applied potential difference and t is the thickness of the piezoelectric.

In (33), the term responsible for the capacitance variation is the first part of the integral, as the second one represents the free capacitance of a parallel plate capacitor, here a piezoelectric sensor. Thus, the capacitance reduction F is given by (34), which if multiplied by 100 gives the percentage of capacitance reduction,

$$F = \frac{\iint_A (d_{31}\sigma_1 + d_{31}\sigma_2 + d_{33}\sigma_3)\, dx\, dy}{V \cdot \frac{\chi_{33}^t \cdot A}{t}} \tag{34}$$

where A is the area of the electrode on the surface of the piezoelectric.

Note that capacitance variation depends on the developed stresses on the surface of the embedded piezoelectric. These stresses vary linearly with the applied voltage V. Thus, in the linear domain, the value of the applied voltage doesn't affect capacitance variation. One of the stresses in the above expression is the out-of-plane stress σ_3, which is one of the reasons behind choosing this numerical tool for the analysis over other commercial tools.

Numerical Assessment

In order to prove the reliability of our numerical model, an assessment was carried out by solving the closed form solution problem proposed by Heyliger (1994) of a thick simply supported plate of thickness to ratio $a/h = 4$ in the sensor configuration. The boundary conditions as well as material orientation can be found in Figure 2. The

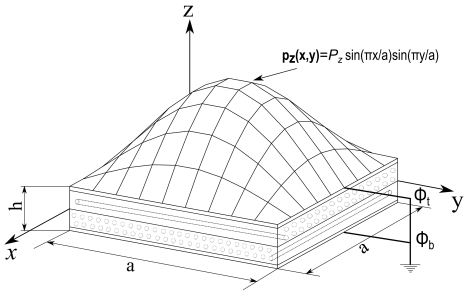

Figure 2. loading and boundary conditions of the thick plate in sensor configuration

Property	PZT-4	Gr/Ep
E_1 (GPa)	81.3	132.38
E_2 (GPa)	81.3	10.756
E_3 (GPa)	64.5	10.756
ν_{12}	0.329	0.24
ν_{13}	0.432	0.24
ν_{23}	0.432	0.49
G_{44} (GPa)	25.6	3.606
G_{55} (GPa)	25.6	5.6537
G_{66} (GPa)	30.6	5.6537
e_{15} (C/m^2)	12.72	0
e_{24}(C/m^2)	12.72	0
e_{31} (C/m^2)	-5.2	0
e_{32} (C/m^2)	-5.2	0
e_{33} (C/m^2)	15.08	0
ϵ_{11}/ϵ_0	1475	3.5
ϵ_{22}/ϵ_0	1475	3.0
ϵ_{33}/ϵ_0	1300	3.0

Table 1. Piezoelectric and dielectric properties of the materials used Heyliger (1994)

material properties of PZT-4 and Gr/Ep materials used in the assessment are found in Table 1. The results of this assessment were compared with the exact results found in the latter mentioned paper.

A convergence analysis was carried out to assess the effects of both mesh refinement and the through-the-thickness expansion. Tables 2 and 3 give the variation of electric potential and in-plane stress σ_{yy} respectively at the center of the square plate. This variation was calculated by obtaining the results of our MUL2 model for the different to the thickness elements, in each of the

mesh	expansion	DOF	$\Delta\phi(\%)$
5 x 5	B2	2420	-1.0461
	B3	4356	-0.4930
	B4	6292	-0.0889
10 x 10	B2	8820	-1.4384
	B3	15876	-0.3115
	B4	22932	-0.0443
20 x 20	B2	33620	-1.3161
	B3	60516	-0.3599
	B4	87412	-0.0355

Table 2. electric potential percentage variation $\Delta\Phi$(a/2,b/2,0) in sensor configuration

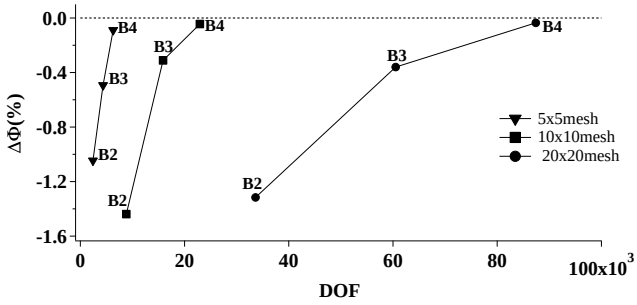

Figure 3. The effect of mesh and through-the-thickness refinement on electric potential variation Φ(a/2,b/2,0)

proposed mesh configurations, subtracting the values found in Heyliger (1994) and multiplying the result by 100. The corresponding Figures 3 and 4 clearly show the results of the voltage and the in-plane stress refinement, accounting for the different refinement parameters and eventually the degree of freedom (DOF) of the problem. It can be shown that the most accurate results are the ones corresponding to the higher mesh refinement (20×20) and for the higher order cubic expansion through-the-thickness (B4 elements). Note that in this study only one through-the-thickness element was assigned to each layer. Stacking more elements to the thickness in each layer would lead to a further higher refinement and better accuracy, but always on the expense of a higher computational cost.

The results of our model, under a fixed refined mesh (20×20), were compared to the closed form solution results in Heyliger (1994) denoted in this paper by 3D results. The results of Tables 4, 5 and 6 respectively showing the electric potential, in-plane stress σ_{yy} and the normal stress σ_{zz} distribution through-the-thickness were plotted in Figures

mesh	expansion	DOF	$\Delta\sigma_{yy}(\%)$
5 x 5	B2	2420	5.0049
	B3	4356	-1.5075
	B4	6292	-1.4072
10 x 10	B2	8820	7.4078
	B3	15876	0.5419
	B4	22932	0.6284
20 x 20	B2	33620	6.8302
	B3	60516	0.0616
	B4	87412	0.1504

Table 3. in-plane stress percentage variation $\Delta\sigma_{yy}$(a/2,b/2,h/2) in sensor configuration

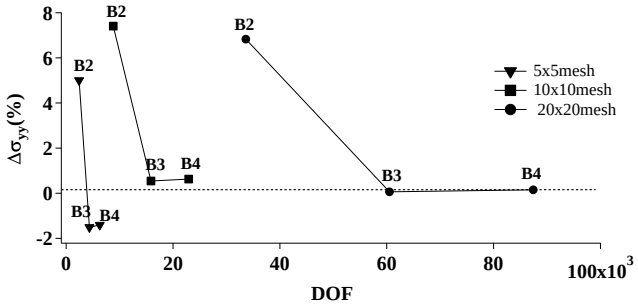

Figure 4. The effect of mesh and through-the-thickness refinement on in-plane stress variation σyy(a/2,b/2,h/2)

5, 6 and 7 to compare the different through-the-thickness expansions with the closed form solution results.

It is shown in Figure 5 that our model can correctly evaluate the electrical component ϕ through-the-thickness. It is also shown that B3 and B4 results are closer to the exact results than B2 results. In Figure 6, it is shown that the model can evaluate the mechanical stress σ_{yy}, where also the B3 and B4 results are closer to the exact results. In Figure 7, it can be shown that B3 and B4 results are close to the exact results. However, the results of B2 expansion are less accurate.

As a conclusion, we can safely say that the electro-mechanical model in hand is quite accurate and is capable of evaluating both the electrical and mechanical variables of the problem in hand. It can also evaluate the out of plane variables in a plate model, which is hard for most other plate modelling software.

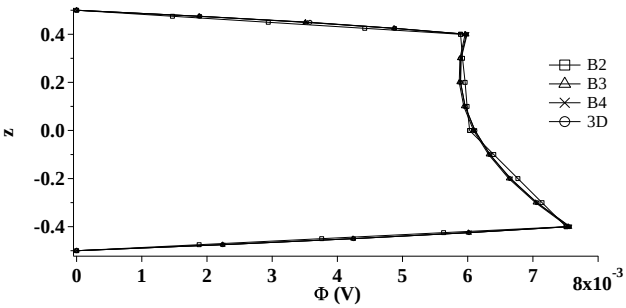

Figure 5. Through-the-thickness distribution of the electric potential ϕ(a/2,b/2)

electric potential ϕ (a/2,b/2) (V)				
z	B2	B3	B4	exact
0.500	0.00000	0.00000	0.00000	0
0.475	0.00147	0.00188	0.00189	0.00189
0.450	0.00294	0.00351	0.00352	0.00358
0.425	0.00442	0.00487	0.00488	0.00488
0.400	0.00589	0.00596	0.00599	0.00598
0.400	0.00589	0.00596	0.00599	0.00598
0.300	0.00592	0.00588	0.00590	0.00589
0.200	0.00596	0.00587	0.00589	0.00589
0.100	0.00599	0.00594	0.00596	0.00596
0.000	0.00603	0.00609	0.00611	0.00611
0.000	0.00603	0.00609	0.00611	0.00611
-0.100	0.00640	0.00632	0.00634	0.00634
-0.200	0.00677	0.00663	0.00666	0.00665
-0.300	0.00714	0.00704	0.00706	0.00706
-0.400	0.00751	0.00754	0.00757	0.00756
-0.400	0.00751	0.00754	0.00756	0.00756
-0.425	0.00563	0.00601	0.00603	0.00602
-0.450	0.00376	0.00424	0.00425	0.00425
-0.475	0.00188	0.00224	0.00225	0.00224
-0.500	0.00000	0.00000	0.00000	0

Table 4. Electric potential distribution ϕ through-the-thickness at (a/2, b/2) in sensor configuration

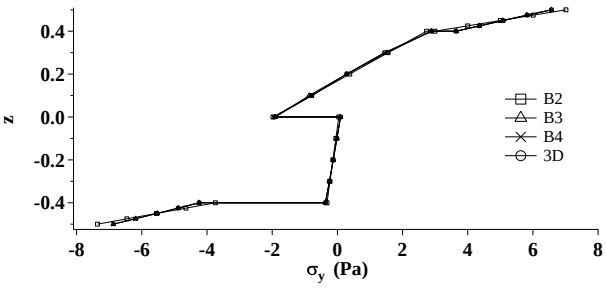

Figure 6. Through-the-thickness distribution of the in-plane stress σ_{yy}(a/2,b/2)

normal stress σ_{yy} (a/2,b/2) (Pa)				
z	B2	B3	B4	exact
0.500	7.01265	6.56834	6.57417	6.5643
0.475	6.00774	5.80997	5.83007	5.8201
0.450	5.00243	5.07007	5.09565	5.0855
0.425	3.99711	4.34895	4.36874	4.3595
0.400	2.99220	3.64688	3.64721	3.6408
0.400	2.73480	2.88392	2.89446	2.8855
0.300	1.55677	1.53142	1.45116	1.4499
0.200	0.37862	0.28197	0.28631	0.2879
0.100	-0.79952	-0.86430	-0.78166	-0.7817
0.000	-1.97649	-1.90639	-1.93324	-1.9266
0.000	0.04400	0.09226	0.10277	0.0991
-0.100	-0.04618	-0.01242	-0.01735	-0.0149
-0.200	-0.13645	-0.12426	-0.12875	-0.128
-0.300	-0.22672	-0.24317	-0.24183	-0.2426
-0.400	-0.31699	-0.36914	-0.36712	-0.3616
-0.400	-3.74207	-4.24579	-4.24363	-4.2348
-0.425	-4.64606	-4.87562	-4.89210	-4.8806
-0.450	-5.55042	-5.52377	-5.54589	-5.5337
-0.475	-6.45477	-6.18999	-6.20695	-6.1951
-0.500	-7.35876	-6.87401	-6.87720	-6.8658

Table 5. In-plane stress distribution σ_{yy} through-the-thickness at (a/2, b/2) in sensor configuration

normal stress σ_{zz} (a/2,b/2) (Pa)				
z	B2	B3	B4	exact
0.500	2.35729	1.02710	1.00153	1
0.475	1.66874	0.99575	0.99875	0.99657
0.450	0.97992	0.97738	0.99058	0.98682
0.425	0.29110	0.97200	0.97535	0.97154
0.400	-0.39745	0.97961	0.95139	0.95151
0.400	0.86500	0.97814	0.96196	0.95151
0.300	0.79354	0.84500	0.84834	0.85199
0.200	0.72207	0.72491	0.73780	0.73747
0.100	0.65059	0.61790	0.62105	0.61686
0.000	0.57919	0.52404	0.48896	0.49831
0.000	0.39870	0.48327	0.50634	0.49831
-0.100	0.33492	0.37828	0.37660	0.38045
-0.200	0.27108	0.26818	0.26092	0.26137
-0.300	0.20723	0.15308	0.15122	0.14821
-0.400	0.14339	0.03299	0.03927	0.04868
-0.400	1.25994	0.02114	0.04847	0.04868
-0.425	0.63983	0.02756	0.02435	0.02845
-0.450	0.01948	0.02179	0.00900	0.01312
-0.475	-0.60088	0.00384	0.00093	0.0034
-0.500	-1.22098	-0.02627	-0.00137	0

Table 6. Normal stress distribution σ_{zz} through-the-thickness at (a/2, b/2) in sensor configuration

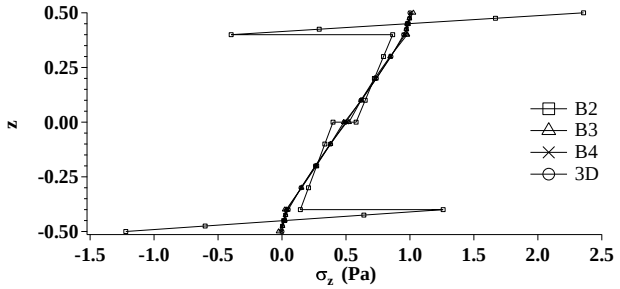

Figure 7. Through-the-thickness distribution of the normal stress σ_{zz}(a/2,b/2)

Property	PZT-5A[a]	PZT-5H[a]	PMN-PZT[b]	PMN-33%PT[c]
C_{11} (GPa)	120	127	117	115
C_{12} (GPa)	75.2	80.2	106	103
C_{13} (GPa)	75.1	84.7	101	102
C_{33} (GPa)	111	117	107	103
C_{44} (GPa)	21	23	56	69
C_{66} (GPa)	22.5	23.5	38	66
d_{31} (pm/V)	-171	-274	-718	-1330
d_{33} (pm/V)	374	593	1530	2820
$\epsilon_{33}^T/\epsilon_0$	1700	3400	4850	8200
$\epsilon_{33}^S/\epsilon_0$	826	1433	590	680

Table 7. Elastic, piezoelectric and dielectric properties of the piezoceramics used, Erturk and J.Inman (2011)[a], Zhang et al. (2008) [b] and Cao et al. (2004) [c]

Capacitance variation of embedded sensors

After evaluating the numerical model and stating the governing equations, the capacitance change of embedded piezoelectric transducers was assessed. The capacitance change was calculated according to (34). The same models given by Elvin et al. (2018) were considered in order to obtain the most comparable results possible.

Effects of the active and host material properties

A plate model with 6 B4 elements through-the-thickness was used to model four different piezoelectric disks, each embedded in isotropic material of different elastic moduli (Ym) and a fixed Poisson ratio $\nu = 0.3$. The host material was modelled to be relatively infinite compared to the size of the embedded disk, where the host material

dimensions are 100 times that of the embedded disk Figure 8, with $a = 300mm, H = 20mm, r = 3mm$ and $2h = 0.2mm$. Symmetric boundary conditions were applied at the borders and the bottom of the plate was restricted to move in the z direction. The plate model shown in Figure 9 was finely meshed the area where the transducer was embedded (24 elements) whereas a coarse mesh was used further away (120 elements). Only a quarter of the plate was modelled and a potential difference of $1V = V_{bottom} - V_{top}$ was imposed between the armatures of the embedded transducer. The mechanical and electrical properties of the embedded transducers used are given in Table 7.

The results of capacitance reduction of the different piezo-electric transducers are given in Table 8 as a function of host material stiffness. These results are plotted both in Figure 10 that shows a close comparison for PZT-5A and PZT-5H piezoelectric transducers and in Figure 11 that provides a comparison between PMN-33%PT and PMN-PZT. The results show that the capacitance reduction increases as the host material stiffness increases. It increases rapidly at first until reaching a stable value where little increase can be seen. Different piezoelectric materials reach different asymptotes depending on the coupling coefficients associated with each. Compared to the results of Elvin et al. (2018) represented in dotted lines, a similar behaviour in capacitance reduction can be shown for the different transducers. The slight difference in values could be due to some differences in the imposed boundary conditions as well as due to the effects of the out-of-plane variable σ_{zz} on capacitance variation.

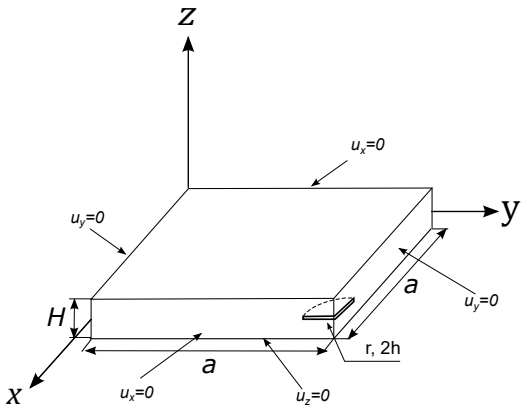

Figure 8. Plate model of the embedded transducer in an infinitely-large host material with the applied plane boundary conditions

Host Ym (GPa)	capacitance reduction (%) PZT-5A	PZT-5H	PMN-PZT	PMN-33%PT
0.1	0.445	0.569	2.612	5.375
1	3.957	5.016	20.082	34.571
5	13.653	16.924	50.827	68.093
10	19.939	24.353	63.184	77.577
20	26.097	31.405	71.956	83.286
40	31.037	36.892	77.234	86.322
80	34.469	40.602	80.086	87.826
160	36.781	43.035	81.606	88.602
320	38.548	44.842	82.548	89.114
640	40.257	46.546	83.336	89.599
1000	41.470	47.745	83.860	89.949

Table 8. Capacitance reduction (%) of different piezo-ceramics as a function of host material elastic modulus

Validation with experimental results from literature

All subsequent analyses carry over from the reference paper presented by Elvin et al. (2018) at which two different results of concern were presented. First, the capacitance reduction from the experimental results, where a square PZT-5A transducer was totally embedded inside an epoxy resin cylinder, and partially embedded in the machined indentation produced on the surface of metallic (steel and Aluminium) rectangular specimens, leaving the upper surface of the transducer exposed at the same level as the host material surface. These results are referred to in this study as 'Experimental results'. Second, the capacitance reduction from the axisymmetric FEM numerical results, where the transducer was modelled as a disk with the same area as the square PZT-5A used in the experimental study, and was modelled fully embedded inside a resin host material disk and partially embedded in metallic host material disks. These results are referred to in this study as 'Numerical FEM results'. In our study, the capacitance reduction of PZT-5A embedded in three different materials is investigated. PZT-5A was fully embedded in the middle of the Epoxy disk structure while partially embedded, mounted just below the surface for Aluminium and Steel structures, Figure12. The properties of the materials used in

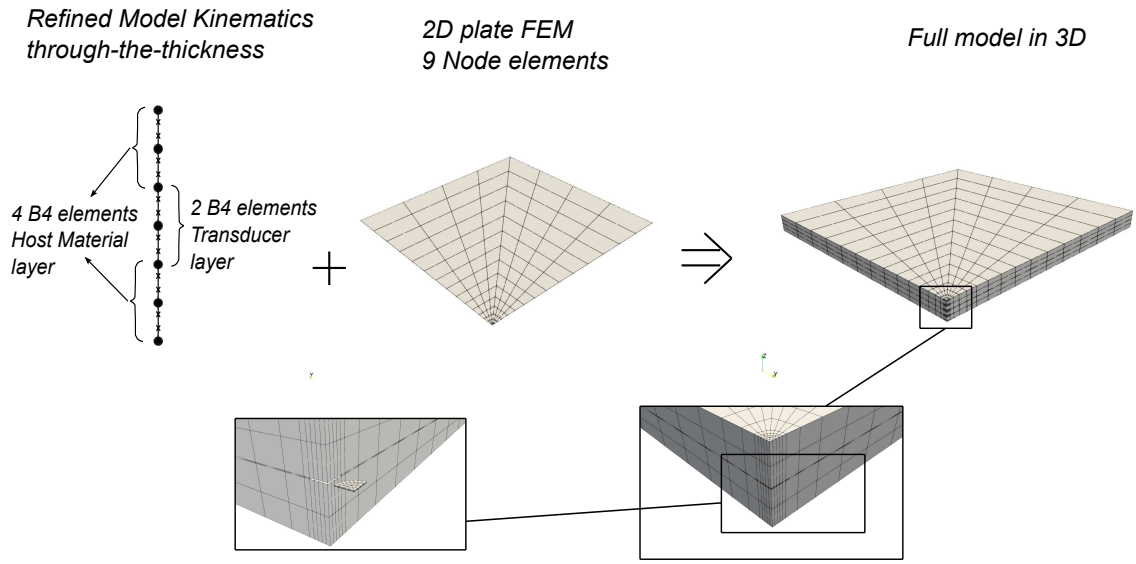

Figure 9. Mesh of the plate model with an embedded transducer in an infinitely-large host material

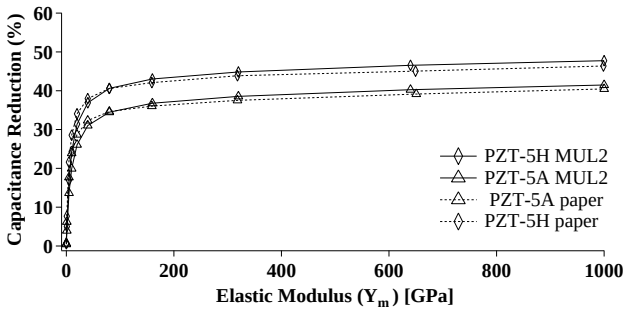

Figure 10. Comparison of embedded capacitance reduction (%) of PZT-5A and PZT-5H, as a function of host material young modulus

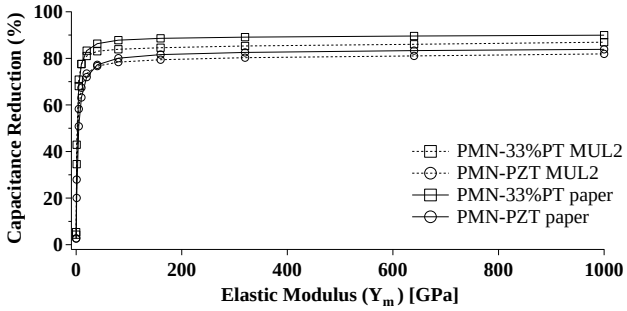

Figure 11. Comparison of embedded capacitance reduction (%) of PMN-33%PT and PMN-PZT, as a function of host material young modulus

this study are found in Table 9. The considered approach in this study is to embed a circular PZT-5A disk of

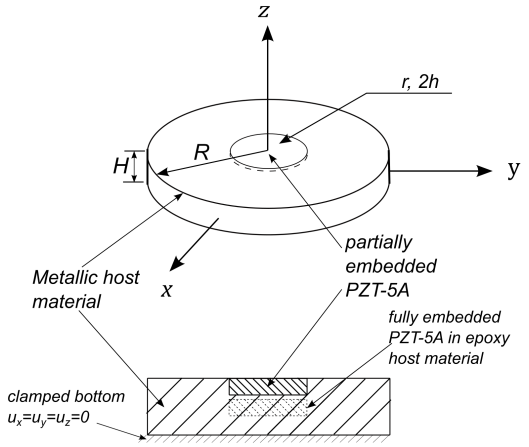

Figure 12. Plate model of the partially embedded transducer in a circular host material, aluminium or steel, under the surface

radius r = 4 mm and 2h = 0.126 mm thickness, (the same model dimensions adopted in the FEM numerical results mentioned in the reference paper), in a circular host material of radius R = 12.5 mm and 6.4 mm thickness while using a plate model with 4 B4 elements though-the-thickness, Figure 12, with a fixed boundary condition on the bottom of the plate. The mesh adopted in this study can be found in Figure 13, where a fine mesh of 108 elements is being used at the center where the transducer is embedded, and a course mesh of 144 elements is being used at the surrounding area.

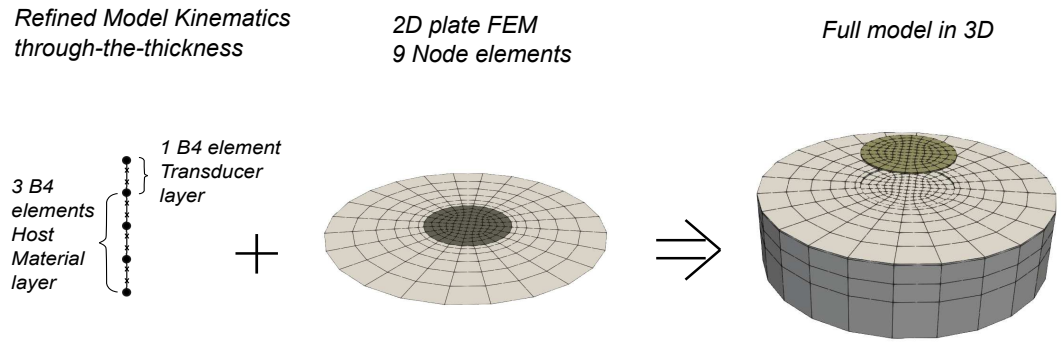

Figure 13. Plate model of the partially embedded transducer in a circular host material, aluminium or steel, under the surface

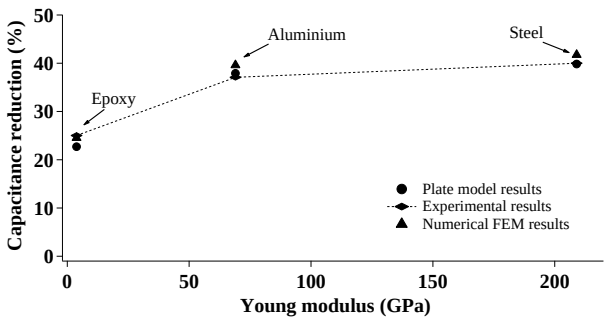

Figure 14. Embedded capacitance reduction $(\%)$ of PZT-5A is different host materials, MUL2 results and results of Elvin et al. (2018) (Experimantal and Numerical FEM results)

Property	PZT-5A	Epoxy	Aluminium	Steel
Y_m (GPa)	-	3.8	69	209
ν (GPa)	-	0.35	0.33	0.3
C_{11} (GPa)	120	-	-	-
C_{12} (GPa)	75.2	-	-	-
C_{13} (GPa)	75.1	-	-	-
C_{33} (GPa)	111	-	-	-
C_{44} (GPa)	21	-	-	-
C_{66} (GPa)	22.5	-	-	-
d_{31} (pm/V)	-190	-	-	-
d_{33} (pm/V)	390	-	-	-
$\epsilon^T_{33}/\epsilon_0$	1700	-	-	-
$\epsilon^S_{33}/\epsilon_0$	826	-	-	-

Table 9. Elastic, piezoelectric and dielectric properties of the materials used in numerical and previous experimental results, Elvin et al. (2018)

Table 10 and Figure 14 show the results of capacitance reduction in both of the mentioned cases above as well as the results of the finite element model and experimental tests in Elvin et al. (2018). It can be shown that the results are close, especially those between the plate model and the experimental results. However, it should be noted that the values of capacitance reduction also vary depending on the shape of the modelled transducer. The difference between the MUL2 models and the numerical model is still due to the same reasons mentioned above, concerning the higher accuracy of the MUL2 model for the out-of-plane variables as well as the possible difference in the applied boundary conditions between our model, and those indistinct conditions adopted by (Elvin et al. 2018) in the experimental study and in the axisymmetric numerical model proposed.

Host Material	capacitance drop $(\%)$		
	MUL2 FEM	Elvin et al. (2018)	
	Plate Model	Experimental results	Numerical FEM results
Epoxy	22.70	25.02	24.54
Al	37.91	37.08	39.61
Steel	39.84	40.00	41.74

Table 10. Capacitance reduction $(\%)$ of PZT-5A embedded in different material, comparison between our results and the results of Elvin et al. (2018)

Impact of the hosting structure thickness

The effect of host material thickness on capacitance reduction was also reproduced using the same plate FEM model in Figure 13 but with different model kinematics, using 9 B4 elements through-the-thickness,Figure 16. The embedded PZT-5A transducer and host material properties

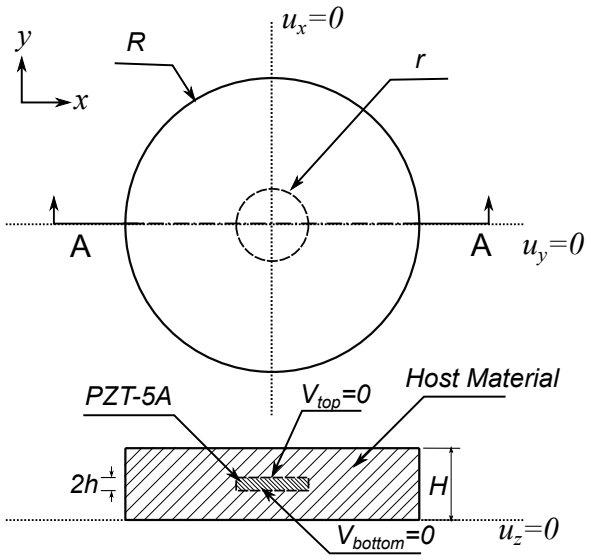

Figure 15. Geometry and Boundary conditions of the model used to study the impact of thickness on capacitance change

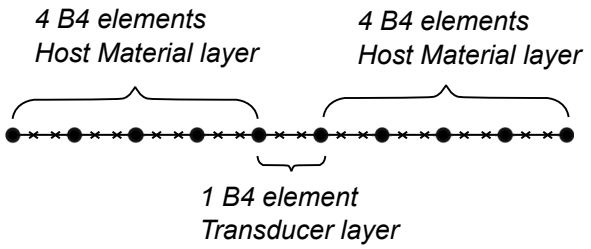

Figure 16. through-the-thickness model kinematics of the plate model used to study the effect of host structure thickness

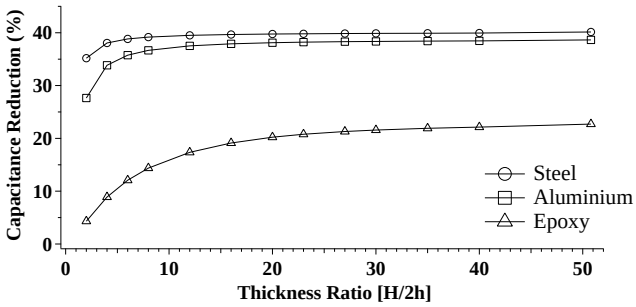

Figure 17. Embedded capacitance reduction (%) of PZT-5A in different materials as a function of host material thickness

H/2h	capacitance reduction (%)		
	Epoxy	Aluminium	Steel
50.79	22.705	38.645	40.141
40	22.132	38.456	39.938
35	21.907	38.414	39.909
30	21.580	38.356	39.874
27	21.302	38.307	39.848
23	20.783	38.214	39.802
20	20.226	38.113	39.756
16	19.128	37.901	39.664
12	17.361	37.512	39.506
8	14.371	36.660	39.173
6	12.076	35.752	38.824
4	8.895	33.835	38.065
2	4.311	27.649	35.181

Table 11. Capacitance reduction (%) of PZT-5A embedded in different materials as a function of host material thickness

used were the same found in Table 9. The in-plane mesh used was the same as that shown in Figure 13 with the transducer embedded at the center. The model geometry and boundary conditions were described in Figure 15, with a PZT radius and thickness respectively fixed at r = 4 mm and 2h = 0.126 mm, embedded at the center of the host material disk. The host material radius is also fixed at R = 12.5 mm but its thickness H is varied between 0.252 mm to 6.4 mm. The results obtained in Table 11 show the capacitance reduction obtained for the different host materials as a function of host to transducer material thickness H/2h.

The results were plotted in Figure 17. As in Elvin et al. (2018), it shows a similar behaviour, with the capacitance reduction increasing rapidly as host to PZT thickness increases until it stabilizes. It is evident that as host material stiffness increases, it stabilizes at a lower thickness ratio, as steel reaches an almost stable capacitance reduction before Aluminium, and the latter before epoxy. In fact, the transducer needs to be embedded in a thicker epoxy host material to reach a stable capacitance, which dictates that capacitance reduction is especially affected by the thickness of epoxy host material. For stiff materials, as steel and aluminium, H $\geq$ 20h is the stabilizing limit whereas for softer materials as epoxy, this limit goes as far as H $\geq$ 80h and beyond.

Conclusion

In this paper, the capacitance variation of embedded piezoelectric sensor has been evaluated using a refined plate model.

The computational model was first assessed to prove its reliability in modelling piezo-electrical problems in the sensor configuration, as capacitance reduction depends on

actuating the embedded PZT. The results, compared to the closed form solution results of Heyliger (1994), show that our model has a good accuracy of estimating the mechanical and electrical variables, especially the out-of-plane stress σ_{zz} and the potential difference through-the-thickness. This is of utmost importance in general and specifically in capacitance reduction application as this reduction depends on the stresses developed on the surface of the embedded transducers.

After the numerical assessment, a qualitative comparison of capacitance reduction between our results and the results in the literature was carried out which shows good correspondence. The effect of coupling coefficients (transducer type), host material stiffness, transducer shape, as well as the host material thickness surrounding the transducer were studied. A closer comparison of the results shows that there is a difference in capacitance reduction values. This could be due to the modelling method adopted in the previous study, as some material properties might be neglected i.e. Shear coefficients of the transducers. It could also be due to the uncertainty of the applied boundary conditions of the previous study or due to some poorly evaluated out-of-plane stresses. All these uncertainties could combine to result in the difference seen. However, the current model can be confidently employed in such areas in the future.

The MUL2 model capabilities were not fully exploited in this study, as node dependent kinematics, which can be used to effectively reduce the computational cost of the problem, enabling kinematics refinement in critical areas while allowing a less refinement in less critical ones, was not addressed. This type of modelling shows a tremendous promise on the scale of large structures with more than one embedded transducer.

Acknowledgements

The authors would like to thank the Hauts-de-France Region (France) and Politecnico di Torino (Italy) for the funding of this work as part of the doctoral thesis of Mr. Jamal NAJD (Agreement number 20003877, N GALIS: ALRC2.0-000072).

This research was funded by the Clean Sky 2 Joint Undertaking under the European Union's Horizon 2020 research and innovation programme, Grant Agreement number: 738078—DEsign, development, manufacture, testing and Flight qualification of nExt geNeration fuel storage system with aDvanced intEgRated gauging and self-sealing capabilities (DEFENDER).

References

Benjeddou A, Trindade M and Ohayon R (1997) A unified beam finite element model for extension and shear piezoelectric actuation mechanisms. *Journal of Intelligent Material Systems and Structures* 8(12): 1012–1025.

Cao H, Schmidt VH, Zhang R, Cao W and Luo H (2004) Elastic, piezoelectric, and dielectric properties of 0.58pb(mg1/3nb2/3)o3-0.42pbtio3 single crystal. *Journal of Applied Physics* 96(1): 549–554.

Carrera E (2003) Theories and finite elements for multilayered plates and shells: a unified compact formulation with numerical assessment and benchmarking. *Archives of Computational Methods in Engineering* 10(3): 215–296.

Carrera E, Brischetto S and Nali P (2011a) *Plates and shells for smart structures: classical and advanced theories for modeling and analysis*, volume 36. John Wiley & Sons.

Carrera E, Cinefra M, Petrolo M and Zappino E (2014) *Finite element analysis of structures through Unified Formulation*. John Wiley & Sons.

Carrera E, Giunta G and Petrolo M (2011b) *Beam structures: Classical and advanced theories*. John Wiley & Sons.

Carrera E and Zappino E (2018) *Node-Dependent Kinematics, Multilayered Beam, Plate, and Shell Elements*. Berlin, Heidelberg: Springer Berlin Heidelberg, pp. 1–14. DOI: 10.1007/978-3-662-53605-6_141-1.

Elvin N, Elvin A and Zamorano Senderos B (2018) Capacitance changes in thin piezoelectric transducers embedded in isotropic host materials. *Journal of Intelligent Material Systems and Structures* 29(5): 816–829.

Erturk A and JInman D (2011) *Piezoelectric Energy Harvesting*. John Wiley & Sons.

Heyliger P (1994) Static behavior of laminated elastic/piezoelectric plates. *AIAA Journal* 32(12): 2481–2484.

Kapuria S and Hagedorn P (2007) Unified efficient layerwise theory for smart beams with segmented extension/shear mode, piezoelectric actuators and sensors. *Journal of Mechanics of Materials and Structures* 2(7): 1267–1298.

Kpeky F, Abed-Meraim F, Boudaoud H and Daya EM (2017) Linear and quadratic solid–shell finite elements SHB8PSE and SHB20E for the modeling of piezoelectric sandwich structures. *Mechanics of Advanced Materials and Structures* DOI:10.1080/15376494.2017.1285466. In press.

M Yaqoob Y, Nazeer A and M Naushad A (2010) Finite element analysis of actively controlled smart plate with patched actuators and sensors. *Latin American Journal of Solids and Structures* 7.

N Ghasemi-Nejhad M, Russ R and Pourjalali S (2005) Manufacturing and testing of active composite panels with embedded piezoelectric sensors and actuators. *Journal of Intelligent Material Systems and Structures* 16(4): 319–333.

Najd J, Harizi W, Aboura Z, Zappino E and Carrera E (2022) Rapid estimation of the fatigue limit of smart polymer-matrix composites (pmc) using the self-heating tests. *Composite Structures* 282: 115039. DOI:https://doi.org/10.1016/j.compstruct.2021.115039.

Nasrollahi A, Deng W, Ma Z and Rizzo P (2018) Multimodal structural health monitoring based on active and passive sensing. *Structural Health Monitoring* 17(2): 395–409.

Reddy J (1999) On laminated composite plates with integrated sensors and actuators. *Engineering Structures* 21(7): 568–593.

Reddy JN (1984) A simple higher-order theory for laminated composite plates. *Journal of Applied Mechanics* 51(4): 745–752.

Reddy JN (2004) *Mechanics of laminated composite plates and shells: theory and analysis*. CRC Press.

Shin S, Zamorano B and Elvin N (2016) Comparison of the electromechanical properties of embedded and surface-mounted piezoelectric transducers. *Journal of Intelligent Material Systems and Structures* 27(20): 2837–2850.

Su Z, Wang X, Chen Z, Ye L and Wang D (2006a) A built-in active sensor network for health monitoring of composite structures. *Smart Materials and Structures* 15(6): 1939–1949.

Su Z, Ye L and Lu Y (2006b) Guided lamb waves for identification of damage in composite structures: A review. *Journal of Sound and Vibration* 295(3): 753–780.

Tang HY, Winkelmann C, Lestari W and La Saponara V (2011) Composite structural health monitoring through use of embedded pzt sensors. *Journal of Intelligent Material Systems and Structures* 22(8): 739–755.

Tuloup C, Harizi W, Aboura Z and Meyer Y (2020) Integration of piezoelectric transducers (pzt and pvdf) within polymer-matrix composites for structural health monitoring applications: new success and challenges. *International Journal of Smart and Nano Materials* 11(4): 343–369.

Tuloup C, Harizi W, Aboura Z, Meyer Y, Khellil K and Lachat R (2019) On the manufacturing, integration, and wiring techniques of in situ piezoelectric devices for the manufacturing and structural health monitoring of polymer–matrix composites: A literature review. *Journal of Intelligent Material Systems and Structures* 30(16): 2351–2381.

Zappino E and Carrera E (2020) Advanced modeling of embedded piezo-electric transducers for the health-monitoring of layered structures. *International Journal of Smart and Nano Materials* 11(4): 325–342.

Zhang S, Luo J, Hackenberger W and Shrout TR (2008) Characterization of pb(in(12)nb(12))o(3)-pb(mg(13)nb(23))o(3)-pbtio(3) ferroelectric crystal with enhanced phase transition temperatures. *Journal of Applied Physics* 104(6).